

**Missing Link between Helical Nano- and Microfilaments in B4 Phase Bent-Core Liquid Crystals, and Deciphering which Chiral Center Controls the Filament Handedness**

*Sasan Shadpour, Ahlam Nemati, Mirosław Salamończyk, Marianne E. Prévôt, Jiao Liu, Nicola J. Boyd, Mark R. Wilson, Chenhui Zhu, Elda Hegmann, Antal I. Jákli, Torsten Hegmann\**

S. Shadpour, A. Nemati, Dr. M. E. Prévôt, J. Liu, Dr. E. Hegmann, Dr. A. I. Jákli, Dr. T. Hegmann  
Chemical Physics Interdisciplinary Program, Advanced Materials and Liquid Crystal Institute,  
Kent State University, Kent (OH) 44242-0001, USA  
E-Mail: thegmann@kent.edu

Dr. M. Salamończyk  
Faculty of Chemistry, University of Warsaw, 02-089 Warszawa, Poland

Dr. N. J. Boyd, Dr. M. R. Wilson  
Department of Chemistry, Durham University, Durham, DH1 3LE, UK

Dr. C. Zhu  
Advanced Light Source, Lawrence Berkeley National Laboratory, Berkeley, CA, 94720, USA

Dr. E. Hegmann  
Department of Biological Sciences, Kent State University, Kent (OH) 44242-0001, USA

Dr. E. Hegmann, Dr. T. Hegmann  
Brain Health Research Institute, Kent State University, Kent (OH) 44242-0001, USA

Dr. A. I. Jákli  
Department of Physics and Astronomy, Kent State University, Kent (OH) 44242-0001, USA

Dr. T. Hegmann  
Department of Chemistry and Biochemistry, Kent State University, Kent (OH) 44242-0001,  
USA

Keywords: bent-core liquid crystals, B4 phases, helical nanofilaments, chirality, handednesses

The range of possible morphologies for bent-core B4 phase liquid crystals has recently expanded from helical nanofilaments (HNFs) and modulated HNFs to dual modulated HNFs, helical microfilaments and heliconical-layered nanocylinders, particularly for a succinct type of bent-core liquid crystals. These new morphologies are observed when one or both aliphatic side chains contain a chiral center. Here, we are addressing the question which of these two chiral centers controls the handedness (helicity) and which the morphology of the nanofilaments formed by bent-core liquid crystals with tris-biphenyl diester core flanked by two chiral 2-octyloxy side chains. The combined results reveal that the longer arm of these non-symmetric bent-core liquid crystals controls the handedness of the resulting dual modulated HNFs. These derivatives with opposite configuration of the two chiral side chains now feature twice as large dimensions compared to the homochiral derivatives with identical configuration. These results are supported by DFT calculations and stochastic dynamic atomistic simulations, which reveal the relative difference between the *para*- and *meta*-sides of the described series of compounds drives the variation in morphology. Finally, X-ray diffraction, SEM, TEM, and AFM data also uncover the new morphology for B4 phases featuring  $p2/m$  symmetry within the filaments and less pronounced crystalline character.

## 1. Introduction

The B4 or helical nanofilament (HNF) phase is an astounding example of self-assembly directed by molecular conformation formed by certain types of bent-core liquid crystals (BCLCs).[1] The phase forms due to an intra-layer mismatch between the two molecular halves that can only be relieved by local saddle-splay, which ultimately leads to twisted filaments composed of a limited number of layer stacks ( $\sim 5$  to 7 layers).[1] In the case of achiral BCLC molecules, HNF phases form a conglomerate composed of macroscopic chiral domains. The classic portrayal of the B4 phase was that of a crystalline phase.[2] More recent work, however, demonstrated that the B4 phase is neither a traditional crystalline solid nor a conventional liquid crystal phase.[3] The porous filaments rather assemble into a loose hexatic liquid crystalline structure.[4, 5]

For a specific class of BCLCs with tris-biphenyl diester (tris-BiPh) central bent-core, subtle modifications of the molecular structure led to the discovery of a modulated HNF phase ( $\text{HNF}_{\text{mod}}$ , **1** in Figure 1) featuring an additional intralayer electron-density modulation[4] and a dual modulated HNF phase ( $\text{HNF}_{\text{mod}2}$ , **2** in Figure 1) with additional intra- as well as interlayer modulations,[6] the latter by introducing chiral centers to both aliphatic chains with identical absolute configuration (homochiral derivatives). Like the HNF and  $\text{HNF}_{\text{mod}}$ , the homochiral  $\text{HNF}_{\text{mod}2}$  phase features a sense-matching secondary twist.[6] We also discovered a heretofore never observed type of polymorphism (defined as the ability of a solid material to exist in more than one form of crystal structure) for such tris-BiPh BCLCs when a single chiral center was exclusively introduced at the *meta*-side of these molecules (**3** in Figure 1). In this case, the formation of entirely different phase structures solely depending on the rate of cooling from the isotropic liquid phase was found. Upon rapid cooling, we discovered a unique new polymorph for B4 phase BCLCs, which we termed helical microfilaments ( $\text{H}\mu\text{Fs}$ ) based on the much larger dimensions of the helical building

blocks. Upon slow cooling, however, an oblique columnar ( $\text{Col}_{\text{ob}}$ ) phase was formed by these materials.[7]

By moving the chiral center to the other side chain, the longer *para*-side of the molecule, we uncovered yet another entirely new morphology for B4 BCLC phases. Unlike the parent molecules with two chiral side chains described thus far or a chiral side chain in the shorter *meta*-side, which form helical nano- or microfilament B4 phases, these derivatives formed heliconical-layered nanocylinders (HLNCs, **4** in Figure 1) composed of up to ten coaxial heliconical layers, which can split or merge, braid, and self-assemble into a variety of modes including feather-like, herringbone, concentric rings, or empty nest-like structures, largely controlled by selecting specific sample thicknesses and appropriate substrates.[8]

Overall, this body of work showed that introducing very subtle structural changes in a set of such tris-BiPh B4 BCLC molecules leads to an exceptionally rich, unprecedented structural and shape polymorphism. In essence, repositioning one or two methyl groups, thereby strategically introducing chiral centers, results in the formation of  $\text{HNF}_{\text{mod}2\text{S}}$ ,  $\text{H}\mu\text{Fs}$  and HLNCs. While the overall conformation of these specific BCLC molecules appears to drive the morphology, it is yet unclear which chiral side chain controls the handedness of the HNFs particularly in those cases with two chiral side chains.

<Figure 1 near here>

To explore this, we here present the synthesis and complete characterization of two new members of the tris-BiPh series with opposite configuration of the two chiral centers in the two chiral 2-octyloxy aliphatic side chains ( $(^mR,^pS)$ -**5** and  $(^mS,^pR)$ -**5** with the opposite configuration of the two chiral centers; Figure 2). The as-synthesized, purified materials were studied by polarized optical microscopy (POM), differential scanning calorimetry (DSC), thin-film circular dichroism (CD) spectropolarimetry, X-ray diffraction (XRD), scanning and

transmission electron as well as atomic force microscopy (SEM, TEM, and AFM). To elucidate the effect of the two chiral centers' configuration on the handedness of the formed HNFs, the results of these experiments were then checked against those obtained earlier for the homochiral as well as racemic members of the series (i.e. ( $^mR,^pR$ )-**2**, ( $^mS,^pS$ )-**2**, and ( $^mrac,^prac$ )-**2** [6]; Figure 2). Finally, we also studied contact preparations between the hetero- and homochiral materials to understand if a matching handedness of the HNFs is a prerequisite for miscibility of HNFs formed by two different compounds. For the homochiral derivatives, for example, such contact preparations indicated the formation of a crystalline columnar phase in the contact zone.[6]

<Figure 2 near here>

## 2. Results and discussion

### 2.1. Polarized optical microscopy

POM investigations provided the first evidence of the single handedness of the HNFs for each of the new compounds. Figure 3 shows the textures, representative for both new compounds, obtained upon slow cooling and heating (rate: 5 °C min<sup>-1</sup>) for ( $^mR,^pS$ )-**5** sandwiched between two pre-cleaned glass substrates.

These thin film textures appear characteristic for an HNF B4 phase at the phase transition from the isotropic liquid phase on cooling, nucleating randomly and growing radially outwards similar to spherulitic domains described previously.[5] Decrossing the polarizers does not change the brightness of any of the domains, indicating the formation of single handedness HNFs (Figures 3c – 3e; for additional images see SI, Figure S3). Interestingly, the HNF phase is the only phase observed on cooling. On heating, however, an

additional phase is formed in a  $\sim 14$  °C temperature interval above the HNF phase, which is characterized by thin film textures typically observed for oblique columnar (Col<sub>ob</sub>) phases (Figure 3b).[7, 8] DSC measurements performed for both compounds, (*mR,pS*)-**5** and (*mS,pR*)-**5**, performed at the same heating/cooling rate ( $5$  °C min<sup>-1</sup>, see SI, Figure S4), confirm the number of phase transitions on heating and cooling, respectively. A comparison of the phase transition enthalpies with those of compound **1**, which displays a related Col — B4 phase sequence ((*mR,pR*)-**2** and (*mS,pS*)-**2** do not), reveals that the enthalpy values for (*mR,pS*)-**5** and (*mS,pR*)-**5** are significantly lower than those recorded for compound **1**. This already indicates a different, less ordered structure of the B4 phase morphology formed by the two enantiomeric compounds (*mR,pS*)-**5** and (*mS,pR*)-**5**.

<Figure 3 near here>

## 2.2. Contact preparations

We also investigated contact preparations by POM between (*mR,pR*)-**2** and (*mS,pR*)-**5** as well as (*mR,pS*)-**5**. The assumption here was that only right-handed HNFs formed by each compounds will show a continuum in the texture and that opposite HNFs would not mix in the contact zone as reported earlier for the two homochiral derivatives (*mS,pS*)-**2** and (*mR,pR*)-**2**. [6] As shown in Figures 4a – 4c, the right-handed HNFs formed by (*mR,pR*)-**2** and (*mS,pR*)-**5** show a continuation and no new phase or discontinuation in the contact zone (*i.e.* the horizontal center of each image), while the contact zone between (*mR,pR*)-**2** and (*mR,pS*)-**5** (Figures 4d – 4f) show a discontinuation. Here, the direct contact between HNFs with opposite handedness (left-handed for (*mR,pS*)-**5** and right-handed for (*mR,pR*)-**2**) results in the formation of a non- or very low birefringent band with just a few small bright dots. Contrary

to the contact zone between left-handed HNFs formed by ( $^mS,^pS$ )-**2** and right-handed HNFs formed by ( $^mR,^pR$ )-**2**, however, no new phase appears to be induced in the current case.

<Figure 4 near here>

### 2.3. X-ray diffraction

To characterize the structure of the low-temperature B4 phase formed by both new compounds, we performed X-ray diffraction (XRD) experiments. A graphical summary of the obtained XRD data is shown in Figure 5. Plot I (Figures 5a and 5b) shows a diffraction pattern of the sample at room temperature after one heating/cooling cycle used to fill the capillary. The low- $q$  maxima indicate a layer structure similar to other B4 phases but lacks the typical non-commensurate high- $q$  maxima signifying the commonly observed crystalline nature of HNF phases.[9] The three low- $q$  maxima at  $q_1$  (001) = 0.171 Å<sup>-1</sup>,  $q_2$  (002) = 0.310 Å<sup>-1</sup>, and  $q_3$  (003) = 0.455 Å<sup>-1</sup>, and the periodicities calculated from these  $q$  values do not indicate a simple layer structure, but rather a layer structure with 36.74 Å periodicity and in-plane order (*i.e.* modulation, as for the HNF<sub>mod</sub> phase [4]). On subsequent heating, the pattern significantly changes (plot II, Figures 5a and 5b), and the observed maxima at 115 °C are best indexed with a strongly interdigitated, monoclinic columnar phase (Col<sub>ob</sub>-P2, 3-dimensional) with lattice parameters of  $a = 28.5$  Å,  $b = 6.33$  Å,  $c = 30.4$  Å, and  $\beta = 108^\circ$  (see model in Figure 5e). Considering the length of molecules (~ 44 Å) and that the cell parameters match to ~ 2/3 of the length of molecule, the aromatic part of the molecules here participates in formation of the core of the columns. The aliphatic side chains are interdigitated with neighboring columns, and the molecules are tilted with respect to a layer normal by ~ 55°. The significant number of sharp high- $q$  peaks indicates the crystalline nature of this particular phase. A similar pattern and phase assignment has recently been made for closely related tris-

biphenyl BCLCs with identical side-chain length but featuring only one chiral center in the longer *para*-side.[8] Additional synchrotron small-angle X-ray scattering (SAXS) experiments (in agreement with the data shown in plot II) were used to clearly index the Col<sub>ob</sub> phase (Figure S5, SI).

<Figure 5 near here>

After heating to the isotropic liquid phase and subsequent cooling at a rate 5 °C min<sup>-1</sup> plots III and IV were obtained at 95 °C and at room temperature, respectively. Both plots show maxima quasi matching the pattern obtained in plot I (as indicated by the red dashed lines), but the lowest-*q* maxima in plots III and IV appear to be composed of multiple overlapping signals (see deconvolution of the broad scattering maxima centered at ~ 0.17 Å<sup>-1</sup> in Figures 5c and 5d). The low-*q* region for this phase resembles the patterns obtained for the crystalline ribbon phase formed by the derivative with two racemic chiral centers (*<sup>m</sup>rac,<sup>p</sup>rac*)-**2** as for plot I.[6] Furthermore, the absence of non-commensurate high-*q* peaks, the presence of a broad diffuse halo in the range from 1.0 to 1.6 Å<sup>-1</sup>, and the unusual larger width of the low-*q* peaks now strongly suggest that this phase is not a traditional B4 phase with pronounced crystalline character, but a more liquid or with respect to the aliphatic side chains amorphous B4 phase with a heretofore not reported dual modulation within and among the layers similar to the correlated crystalline ribbons observed for the racemic derivative mixture (*<sup>m</sup>rac,<sup>p</sup>rac*)-**2** (mixture of (*<sup>m</sup>R,<sup>p</sup>R*), (*<sup>m</sup>S,<sup>p</sup>S*), (*<sup>m</sup>R,<sup>p</sup>S*), and (*<sup>m</sup>S,<sup>p</sup>R*) statistically at 25% by weight each). The structure at room temperature and at 95 °C (plots III and IV) is commensurate with a lamellar (or 2D Col<sub>ob</sub>) phase with a cell parameter *c* comparable to the length of the molecules, suggesting a less dense packing of molecules (Figure 5f). The model proposed is a monoclinic structure with *p2/m* symmetry and unit cell parameters of *a* = 40.1 Å, *c* = 43.1 Å,

and  $\beta = 105^\circ$ , which would indeed point to a new B4 phase morphology with more pronounced liquid-like character.

#### 2.4. Thin-film CD experiments

The next set of the experiments was carried out by thin film CD spectropolarimetry (film thickness: 10  $\mu\text{m}$ ). Thin film CD has proven to be an invaluable tool for examining the formation of B4 phases with various morphologies. Among these, the homochiral HNF<sub>mod2</sub> morphology displayed strong thin film sum-CD bands around 350 nm with positive or negative sign depending solely on the handedness of the twisted layers stacked into HNFs, or additionally due to the formation of a secondary twist depending on the handedness of individual HNFs.[6, 10, 11]

The individual thin film linear dichroism spectra for (*mR,pS*)-**5** and (*mS,pR*)-**5** collected on slow cooling (5  $^\circ\text{C min}^{-1}$ ) from the isotropic liquid phase at different sample rotation angles and the resulting sum thin film CD spectra (note that the sum of the collected spectra cancels out the contribution of linear dichroism and birefringence giving rise to real thin film CD data) are shown in Figure 6. Both compounds show intense, characteristically structured thin film sum-CD signals with bands centered around 357 nm for (*mR,pS*)-**5** and 336 nm for (*mS,pR*)-**5**. The mirror image relationship of these sum-CD spectra, despite the  $\sim 20$  nm discrepancy in the sum peak wavelength maxima, evidently indicates the opposite handedness of the HNFs. The shift in wavelength appears to be the result of slight variations in sample thickness, by slanting or variation from sample to sample, despite the use of nominal spacers between the two quartz substrates. These thin film CD spectra are a combination of CD absorption and reflection spectra due to the blue structural color. Correlating the sign of these sum-CD bands to the specific handedness previously determined for the two homochiral HNF<sub>mod2</sub> materials, (*mR,pR*)-**2** and (*mS,pS*)-**2**, [6] already seems to indicate that the positive band for (*mR,pS*)-**5** (Figure 6a) and the negative band for (*mS,pR*)-**5** (Figure 6b) are the result of

the handedness (chirality of the HNFs) being controlled by the chiral center in the longer arm (*para*-side) of these BCLC molecules. If correct, the positive band for the two compounds with an (*S*)-chiral center in the longer *para*-side ( $(^mS,^pS)$ -**2** and  $(^mR,^pS)$ -**5**) would be the result of left-handed  $\text{HNF}_{\text{mod}2S}$  and the negative band for the two compounds with an (*R*)-chiral center in the longer *para*-side ( $(^mR,^pR)$ -**2** and  $(^mS,^pR)$ -**5**) the result of right-handed HNFs.[6] Solution CD spectra recorded in toluene at a concentration where  $(^mR,^pS)$ -**5** and  $(^mS,^pR)$ -**5** form gels ( $\sim 4 \text{ mg mL}^{-1}$ ) consisting of dilute nanofilament (apparent by the faint blue structural color) show typical solution CD spectra with mirror imaged CD couplets (Figure S6) crossing zero at 350 nm.

<Figure 6 near here>

## 2.5. Imaging (SEM, TEM, and AFM)

To confirm our assumption from the thin-film CD data, we next characterized  $(^mR,^pS)$ -**5** and  $(^mS,^pR)$ -**5** by scanning as well as transmission electron microscopy (SEM and TEM) to visualize the morphology and especially the handedness of the HNFs. Since the B4 phase features crystalline layers[3, 6], we can perform scanning as well as transmission electron microscopy experiments directly (no freeze fracture or cryo-TEM are really necessary). Figure 7 shows the SEM of  $(^mR,^pS)$ -**5** and  $(^mS,^pR)$ -**5** after heating to the isotropic liquid phase and cooling at a rate of  $5 \text{ }^\circ\text{C min}^{-1}$  to room temperature ( $\sim 20 \text{ }^\circ\text{C}$ ). First, each material was imaged as a free surface, revealing the handedness assignment made by thin-film CD was indeed correct, left-handed for  $(^mR,^pS)$ -**5** (Figure 7a) and right-handed for  $(^mS,^pR)$ -**5** (Figure 7c). Considering the XRD data, these SEM images confirm that the low-temperature phase is indeed a dual modulated HNF B4 morphology ( $\text{HNF}_{\text{mod}2}$ ) with in-filament  $c2/m$  symmetry (2D  $\text{Col}_{\text{ob}}$ ) and less pronounced crystalline character.

We further checked the handedness by isolating individual HNFs in the well-defined nanopores ( $\varnothing_{\text{pore}} = 60 \text{ nm}$ ) of commercially available anodic aluminum oxide (AAO) wafers pioneered by Yoon and co-workers.[12-15] The obtained SEM images of the cracked AAO wafers, containing isolated HNFs, confirm the assignment of the handedness made for the bulk free surface samples, but also show filaments with an altered overall shape and a lower helical pitch of about 100 nm (Figures 7b and 7d).

<Figure 7 near here>

Low-dose TEM imaging of isolated HNFs (Figures 8a and 8b) confirm the handedness of the filaments of one of the two compounds, ( $^mS,^pR$ )-**5**, and allowed, more precisely, for measuring the HNF dimensions. These HNFs are characterized by a larger width ( $\sim 100 \text{ nm}$ ) than commonly reported for HNFs ( $\sim 40 \text{ nm}$ ) as well as a longer helical pitch  $p$  ( $\sim 350 - 400 \text{ nm}$ ) as compared to the typical value of  $\sim 200 \text{ nm}$ .[1, 16] Generally, all dimensions of these new types of B4 phase modulated HNFs are about twice as large. The dimensions of the non-confined HNFs measured by SEM image analysis matches these values. Not surprising then, the HNFs under confinement in AAO show smaller values for width and helical pitch, because the pores are smaller than the average HNF width (pore diameter  $\varnothing_{\text{pore}} = 60 \text{ nm}$  vs. width of the non-confined filaments  $w = 100 \text{ nm}$ ), which as a result thereof affects the measured helical pitch and the filament shape as demonstrated by Yoon and co-workers.[15]

<Figure 8 near here>

In addition, we also obtained tapping mode atomic force microscopy (AFM) images (Figure 9). With the sample of ( $^mR,^pS$ )-**5** cooled at a rate of  $5 \text{ }^\circ\text{C min}^{-1}$  at from the isotropic liquid phase to room temperature ( $\sim 20 \text{ }^\circ\text{C}$ ), the HNFs with average width and helical pitch

matching the values obtained by SEM image analysis ( $\sim 100$  nm width and  $\sim 350$  nm helical pitch) these AFM images [17] also confirm the left-handedness for ( $^mR,^pS$ )-**5**.

*<Figure 9 near here>*

## 2.5. DFT calculations and stochastic dynamic atomistic simulations

The geometry of compounds ( $^mR,^pS$ )-**5** and ( $^mS,^pR$ )-**5** were optimized in vacuum using DFT methods and the B3LYP functional, combined with the 6-311G(d,p) basis set. The lowest energy geometries are shown in Figure 10. Both compounds show a very similar energy minimized conformation of the tris-biphenyl molecular core. However, the overall molecular geometry of the optimized structures differs slightly due to the specific projection of the chains at the core-chain junction. The effect of the chiral center on each arm of both ( $^mR,^pS$ )-**5** and ( $^mS,^pR$ )-**5** appears to rotate and bend the alkyl chains out of the plane of the molecular core structure, with the direction of the displacement differing depending on the ( $S$ )- or ( $R$ )- assignment at the chiral centers.

*<Figure 10 near here>*

This is further clarified from the analysis of various dihedral distribution functions obtained from single molecule stochastic dynamics (SD) atomistic simulations for each compound (Figure 11). These were performed in the gas phase at 300 K and for a total of 500 ns using the GAFF-LCFF force field developed previously.[18, 19] Figure 11a shows the selected dihedrals while Figures 11b and 11c display the dihedral distribution functions. It is clear from these data that the ( $S$ )- and ( $R$ ) configurations result in mirror images of the dihedral distribution profiles. The dihedral angles closest to the molecular core,  $\theta_1$ ,  $\theta_2$  and  $\varphi_1$ ,

$\varphi_2$  show a small deviation from the *trans* conformation ( $180^\circ$ ). This is followed by a greater deviation from the *trans* conformation for dihedral angles  $\theta_3$  and  $\varphi_3$  where dominant peaks occur at  $\sim 60^\circ$  (*(S)*-configuration) and  $\sim 300^\circ$  (*(R)*-configuration). Collectively, these dihedral angle distributions adjacent to the molecular aromatic core induce a bend in the core-chain junction and a displacement of the alkyl chain away from the plane of the outer phenyl ring. This results in mirror images of the local topology of the core-chain junction arising from the (*R*)- and (*S*)-configurations.

<Figure 11 near here>

This still does not explain the observation that the chirality of the HNFs is controlled by the chiral center in the longer arm (*para*-side). The only remaining difference between the *para*- and *meta*-side arms of (*<sup>m</sup>R,<sup>p</sup>S*)-**5** and (*<sup>m</sup>S,<sup>p</sup>R*)-**5** is that the *para*-side contains an additional biphenyl torsion. It has been previously noted that bent-core mesogens containing biphenyl units can readily assume twisted conformations that enhance the overall conformational chirality.[20] In this case, it is assumed that the additional biphenyl torsion on the *para*-side contributes to greater conformational chirality and hence helical twisting power for this arm compared with that for the *meta*-side arm. This may explain the dominance of the *para* arm in determining the handedness of the HNFs. Figure 11d shows the dihedral angle distributions for the two biphenyl torsions of the *para*-side of (*<sup>m</sup>S,<sup>p</sup>R*)-**5**. These clearly demonstrate that multiple twisted conformations are possible for this arm. It was noted that the profiles for the remaining biphenyl torsions for both compounds were largely identical to those shown in Figure 11d.

### 3. Conclusions

Previous single molecule stochastic dynamics (SD) atomistic simulations have shown

that the chiral center in the longer *para*-side of compounds **4** promotes a significant shift to lower bend angles between the core and chain compared with compounds **3** with the chiral center in the shorter *meta*-side. These data suggested that the effect of the chiral center in the *para*-side in **4** is to induce a conformational change to a more bent shape at the core-chain junction compared to that for the longer arm lacking a chiral center in **3**. We concluded that the presence of the chiral center on the longer *para*-side exerts a greater influence on the overall molecular shape and chirality of the molecule than when the chiral center is located on the *meta*-side. The dihedral distribution functions suggested that placement of the chiral center on the *para*-side of these molecules appears to further increase the bent-twist nature of this arm, which in turn may enhance the mismatch between the two halves of these BCLC molecules.[8] With this information at hand, it is perhaps not surprising that the relative difference between the *para*- and *meta*-sides of compounds **2** and **5** as well as in the entire series of tris-BiPh BCLCs drives the variation in phase structure and morphology.

<Figure 12 near here>

Furthermore, XRD studies reveal another new internal morphology and TEM imaging larger overall dimensions of this new morphology for these B4 phase materials with opposite configuration of the two chiral centers. XRD data show a monoclinic structure ( $p2/m$  symmetry) and more pronounced liquid crystalline or perhaps amorphous character within the filaments (with respect to the aliphatic chains) based on the absence of non-commensurate high- $q$  maxima, whose presence normally indicates the crystalline nature of HNF B4 morphologies. Unfortunately, however, application of an electric field only resulted in minor changes of the birefringence of the HNF<sub>mod2b</sub> phase at room temperature (Figure S7), but this nonetheless warrants further exploration. TEM shows widths and helical pitch values of the overall HNFs (HNF<sub>mod2b</sub>) that are about twice as large as commonly observed for B4 HNFs

(HNF, HNF<sub>mod</sub>, and HNF<sub>mod2a</sub>), but also about half the values of the H $\mu$ Fs formed by compounds **3** (Figure 12). If the configuration of the longer *para*-side is identical, both HNF<sub>mod2a</sub> and HNF<sub>mod2b</sub> display the same handedness (left-handed for (*S*), right-handed for (*R*)). Identical configurations in the shorter *meta*-side lead to opposite handedness for HNF<sub>mod2bS</sub> and H $\mu$ Fs. Generally speaking, the interplay between the existence and configuration of chiral centers in both the shorter *meta*-side and the longer *para*-side of these molecules controls the morphology (or type and degree of curvature) and the helicity of the formed filaments, and both sides either work together or are antagonistic. Astonishing is the similarity of the formed morphologies to those formed by Gemini surfactants, where interchanging the nature of the counterion, thereby varying the chirality, leads to very similar morphologies with varying degrees and types of curvature, dimensions, and helical pitch.[21] In conclusion, for a given set of these non-symmetric BCLC molecules, more refined design rules can now be formulated that include general phase behavior (sequence), morphology (size, shape, type of curvature), internal structure, as well as control over primary and secondary twist in B4 phase-forming BCLCs.

## 4. Experimental section

### 4.1. Materials

Commercial available materials were used as purchased without any further purification. Unless otherwise stated, all organic solvents used for the synthesis were EMD Millipore grade and purified by a PureSolv solvent purification system (Innovative Technology Inc.). Dichloromethane (CH<sub>2</sub>Cl<sub>2</sub>) and benzene (C<sub>6</sub>H<sub>6</sub>) for syntheses were dried before use with 4-Å molecular sieves overnight. Tetrahydrofuran (THF) was dried over sodium-benzophenone and distilled under a nitrogen atmosphere prior to use. All glassware used for the reactions was dried overnight at 140 °C in an oven. All reagents used were

purchased from Sigma Aldrich except for 4-*n*-octyloxybiphenyl-4'-carboxylic acid (purchased from Synthos Chemicals GmbH & Co. KG) and for 1-ethyl-3-(3-dimethylaminopropyl)carbodiimide (EDCI) (purchased from TCI). Anodic aluminum oxide (AAO) wafers were purchased from InRedox Co.

The synthetic approach for the new compounds (*mR,pS*)-**5** and (*mS,pR*)-**5** (Figure. 1) was described earlier,[6-8] and involves the stepwise deprotection and esterification of mono-tetrahydropyranyl (THP)—mono-TBDMS (*tert*-butyldimethylsilyl)-protected 3,4'-dihydroxybiphenyl, which was synthesized by a Suzuki coupling reaction[22, 23] (for the synthesis scheme and characterization data see Supporting Information, SI, Scheme S1 as well as Figures S1 and S2).

## 4.2. Methods

<sup>1</sup>H NMR (400 MHz) and <sup>13</sup>C NMR (100 MHz) spectra for the synthesized materials were obtained using Bruker Avance 400 MHz spectrometer in CDCl<sub>3</sub>. <sup>1</sup>H NMR spectra are reported in parts per million ( $\delta$ ) relative to residual solvent peaks (7.26 ppm for CDCl<sub>3</sub>). <sup>13</sup>C NMR spectra are reported in parts per million ( $\delta$ ) relative to residual solvent peaks (77.00 for CDCl<sub>3</sub>). Robertson MicroLit Laboratories (Legdewood, NJ) provided elemental analysis. DSC measurements were performed using a PERKIN ELMER Pyris 1 at heating and cooling rates of 5 °C min<sup>-1</sup> as well as 50 °C min<sup>-1</sup>. Temperatures were calibrated with indium and zinc as standards. Polarized optical microscopy (POM) observations were carried out under an Olympus BX-53 polarizing microscope equipped with a Linkam LTS420E heating/cooling stage. CD spectropolarimetry was performed using an OLIS spectrophotometer between quartz substrates. Scanning electron microscopy (SEM) analysis was performed using a Quanta 450 FEG SEM. Transmission electron microscopy (TEM) analysis was performed using JEM-1400Plus (JEOL; Peabody, MA, USA) at 90 kV. Images were taken with a 100 kV side mount camera (Orius; GATAN; Pleasanton, CA, USA). Atomic force microscopy

(AFM) images were taken in tapping mode at room temperature using a Hitachi AFM 5100N. For both electron and atomic force microscopy sample preparations, the materials were dissolved in chloroform. A drop of the solution was placed on either indium tin oxide substrates for SEM or plain glass substrates for AFM. After evaporation of the solvent in vacuum, the sample was heated and cooled as described for the POM experiments. The X-ray diffraction (XRD) data were acquired using a Bruker D8 GADDS system (CuK $\alpha$  line, Goebel mirror, point beam collimator, Vantec2000 area detector). Samples were prepared as droplets on a heated surface controlled by Linkam-THMS-600. Small angle X-ray diffraction (SAXD) experiments were also carried out on beamline 7.3.3 of the Advanced Light Source of Lawrence Berkeley National Laboratory<sup>1</sup> (10 keV incident beam energy, 1.24 Å wavelength, utilizing a Pilatus 2 M detector).[24] The materials were filled into 1 mm diameter quartz X-ray capillary tubes, which were then mounted into a custom-built aluminum cassette that allowed X-ray detection with  $\pm 13.5^\circ$  angular range. The cassette fits into a standard hot stage (Instec) that allowed temperature control with  $\pm 0.1$  °C precision. Analysis was done using Igor Pro software with Nika package.[25]

### **Supporting Information**

Supporting Information is available from the Wiley Online Library or from the author.

### **Acknowledgements**

We thank the University of Warsaw for access to their XRD facilities.

### **Funding**

The work was financially supported by the U.S. National Science Foundation (NSF, DMR-1506018), the Ohio Third Frontier program for Ohio Research Scholars “Research Cluster on Surfaces in Advanced Materials” (T.H.), which also supports the Liquid Crystal Characterization facility at the Liquid Crystal Institute (KSU) where some of the current SEM

data were acquired. We are also grateful for access to the beamline 7.3.3 at the Advanced Light Source (Lawrence Berkeley National Laboratory), which are supported by the Director (Office of Science, Office of Basic Energy Sciences) of the U.S. Department of Energy under Contract No. DE-AC02-05CH11231. N.J.B. and M.R.W. would like to thank Durham University for computer time on its Hamilton HPC facility. M.S. acknowledges the support of the National Science Center (Poland); grant 2016/22/A/ST5/00319.

## References

1. L. E. Hough, H. T. Jung, D. Krueker, M. S. Heberling, M. Nakata, C. D. Jones, D. Chen, D. R. Link, J. Zasadzinski, G. Heppke, J. P. Rabe, W. Stocker, E. Korblova, D. M. Walba, M. A. Glaser, N. A. Clark, *Science* **2009**, *325* (5939), 456-460.
2. G. Pelzl, S. Diele, W. Weissflog, *Adv. Mater.* **1999**, *11* (9), 707-724.
3. D. M. Walba, L. Eshdat, E. Korblova, R. K. Shoemaker, *Cryst. Growth Des.* **2005**, *5* (6), 2091-2099.
4. E. Tsai, J. M. Richardson, E. Korblova, M. Nakata, D. Chen, Y. Q. Shen, R. F. Shao, N. A. Clark, D. M. Walba, *Angew. Chem. Int. Edit.* **2013**, *52* (20), 5254-5257.
5. D. Chen, M. R. Tuchband, B. Horanyi, E. Korblova, D. M. Walba, M. A. Glaser, J. E. MacLennan, N. A. Clark, *Nat. Commun.* **2015**, *6*, 7763.
6. L. Li, M. Salamończyk, A. Jákli, T. Hegmann, *Small* **2016**, *12* (29), 3944-3955.
7. L. Li, M. Salamończyk, S. Shadpour, C. Zhu, A. Jákli, T. Hegmann, *Nat. Commun.* **2018**, *9*, 714.
8. S. Shadpour, A. Nemati, N. J. Boyd, L. Li, M. E. Prévôt, S. L. Wakerlin, J. P. Vanegas, M. Salamończyk, E. Hegmann, C. Zhu, M. R. Wilson, A. I. Jákli, T. Hegmann, *Mater. Horiz.* **2019**, *6*, 959-968.
9. A. Zep, M. Salamończyk, N. Vaupotič, D. Pocięcha, E. Gorecka, *Chem. Commun.* **2013**, *49* (30), 3119-3121.
10. G. Gottarelli, S. Lena, S. Masiero, S. Pieraccini, G. P. Spada, *Chirality* **2008**, *20* (3-4), 471-485.
11. H. Niwano, M. Nakata, J. Thisayukta, D. R. Link, H. Takezoe, J. Watanabe, *J. Phys. Chem. B* **2004**, *108* (39), 14889-14896.
12. H. Kim, S. Lee, T. J. Shin, E. Korblova, D. M. Walba, N. A. Clark, S. B. Lee, D. K. Yoon, *Proc. Natl. Acad. Sci.* **2014**, *111* (40), 14342-14347.
13. S. Lee, H. Kim, E. Tsai, J. M. Richardson, E. Korblova, D. M. Walba, N. A. Clark, S. B. Lee, D. K. Yoon, *Langmuir* **2015**, *31* (29), 8156-8161.
14. S. H. Ryu, H. Kim, S. Lee, Y. J. Cha, T. J. Shin, H. Ahn, E. Korblova, D. M. Walba, N. A. Clark, S. B. Lee, D. K. Yoon, *Soft Matter* **2015**, *11* (39), 7778-7782.
15. S. Lee, H. Kim, T. J. Shin, E. Tsai, J. M. Richardson, E. Korblova, D. M. Walba, N. A. Clark, S. B. Lee, D. K. Yoon, *Soft Matter* **2015**, *11* (18), 3653-3659.
16. C. H. Zhu, C. Wang, A. Young, F. Liu, I. Gunkel, D. Chen, D. Walba, J. E. MacLennan, N. A. Clark, A. Hexemer, *Nano Lett.* **2015**, *15* (5), 3420-3424.
17. M. J. Gim, H. Kim, D. Chen, Y. Q. Shen, Y. Yi, E. Korblova, D. M. Walba, N. A. Clark, D. K. Yoon, *Sci. Rep.* **2016**, *6*, 29111.
18. N. J. Boyd, M. R. Wilson, *Phys. Chem. Chem. Phys.* **2015**, *17* (38), 24851-24865.
19. N. J. Boyd, M. R. Wilson, *Phys. Chem. Chem. Phys.* **2018**, *20* (3), 1485-1496.
20. H. Takezoe, *Liquid Crystals: Materials Design and Self-Assembly* **2012**, *318*, 303-330.
21. R. Oda, I. Huc, M. Schmutz, S. J. Candau, F. C. MacKintosh, *Nature* **1999**, *399* (6736).
22. N. Miyaura, A. Suzuki, *Chem. Rev.* **1995**, *95* (7), 2457-2483.
23. A. A. Thomas, S. E. Denmark, *Science* **2016**, *352* (6283), 329-332.
24. A. Hexemer, W. Bras, J. Glossinger, E. Schaible, E. Gann, R. Kirian, A. MacDowell, M. Church, B. Rude, H. Padmore, *XIV International Conference on Small-Angle Scattering (Sas09)* **2010**, *247*, 012007.
25. J. Ilavsky, *J. Appl. Crystallogr.* **2012**, *45*, 324-328.

## Figure Captions

**Figure 1.** Members of the tris-BiPh diester series with achiral 1-octyloxy or chiral 2-octyloxy side chain(s) and their corresponding B4 phase morphologies.

**Figure 2.** Chemical structure, phase sequence, and morphology (of the B4 phase) recorded at a constant heating/cooling rate of  $5\text{ }^{\circ}\text{C min}^{-1}$  (phase transition temperatures from 2<sup>nd</sup> heating/cooling run by DSC. The pink curved arrows indicate the handedness of the  $\text{HNF}_{\text{mod}2\text{S}}$  depending on the configuration of the involved chiral centers in both aliphatic side chains. Superscript letters *m* (for *meta*) and *p* (for *para*) indicate the configuration of the chiral center at the *meta*- and *para*-side of the BCLC molecules, respectively.

**Figure 3.** Polarized optical micrographs (polarizer and analyzer as indicated by arrows in the upper right corner of each image) for (*mR,pS*)-**5** sandwiched between two clean glass substrates with  $10\text{ }\mu\text{m}$  spacers at a constant heating/cooling rate of  $5\text{ }^{\circ}\text{C min}^{-1}$ : (a) at room temperature ( $\sim 20\text{ }^{\circ}\text{C}$ ) on cooling from the isotropic liquid phase, (b) at  $117\text{ }^{\circ}\text{C}$  on heating, and (c-e) on heating at  $90\text{ }^{\circ}\text{C}$  with varying polarizer/analyzer positions. Scale bars are  $100\text{ }\mu\text{m}$  each.

**Figure 4.** Polarized optical photomicrographs (polarizer and analyzer position as indicated by arrows in the upper right corner of each image) of contact preparations between: (a-c) (*mR,pR*)-**2** on the right and (*mS,pR*)-**5** on the left, and (d-f) (*mR,pR*)-**2** on the right and (*mR,pS*)-**5** on the left. After ensuring contact and mixing in the contact zone (highlighted by yellow dashed lines), samples, sandwiched between two clean glass substrates, were first heated to the isotropic liquid phase and subsequently cooled at a constant rate of  $5\text{ }^{\circ}\text{C min}^{-1}$  from the isotropic liquid phase to room temperature ( $\sim 20\text{ }^{\circ}\text{C}$ ); scale bars are  $100\text{ }\mu\text{m}$  each. The difference in birefringence between compounds **2** and **5** in some cases required adjustment of the light intensity (depending on the sample thickness), which resulted particularly for images (a) to (c) in less bright photomicrographs compared to those shown in (d) to (f) and in Figure 3.

**Figure 5.** X-ray diffraction analysis of (*mR,pS*)-**5** on heating and cooling (at 5 °C min<sup>-1</sup>): (a) azimuthally integrated intensity (a.u.) vs.  $q$  (Å<sup>-1</sup>) and (b) the corresponding 2D diffraction patterns. Plot I: (100) = 0.171 Å<sup>-1</sup>, (002) = 0.310 Å<sup>-1</sup>, and (003) = 0.455 Å<sup>-1</sup>; plot II: (001) = 0.218 Å<sup>-1</sup>, (100) = 0.2368 Å<sup>-1</sup>, (101) = 0.365 Å<sup>-1</sup>, (002) = 0.4365 Å<sup>-1</sup>, (200) = 0.4649 Å<sup>-1</sup>, (010) = 0.5494 Å<sup>-1</sup>, (105) = 0.577 Å<sup>-1</sup>, and (60 $\bar{2}$ ) = 0.6586 Å<sup>-1</sup>; plot III with deconvoluted low- $q$  (001) maxima shown in (c) plot III:  $q_{1a}$  (001) = 0.1489 Å<sup>-1</sup>,  $q_{1b}$  (100) = 0.1713 Å<sup>-1</sup>, and  $q_{1c}$  (10 $\bar{1}$ ) = 0.2122 Å<sup>-1</sup>, (002) = 0.303, (200) = 0.325, (003) = 0.453, and (004) = 0.603 and for and plot IV with deconvoluted low- $q$  shown in (d):  $q_{1a}$  (001) = 0.1524 Å<sup>-1</sup>,  $q_{1b}$  (100) = 0.1751 Å<sup>-1</sup>, and  $q_{1c}$  (10 $\bar{1}$ ) = 0.1937 Å<sup>-1</sup>, (002) = 0.303, (200) = 0.325, (003) = 0.454, and (004) = 0.603. Corresponding molecular models for: (e) the Col<sub>ob</sub> phase and (f) the B4 HNF<sub>mod2b</sub> phase as calculated from the data obtained from plot IV for which the X-ray exposure time was the longest.

**Figure 6.** Thin film CD spectra (individual sample rotation angles, i.e. linear dichroism spectra, and sum-CD spectra; film thickness: 10 μm) of: (a) (*mR,pS*)-**5** and (b) (*mS,pR*)-**5** taken after slow cooling from the isotropic liquid phase at a rate of 5 °C min<sup>-1</sup> at room temperature (~ 20 °C) in the B4 phase.

**Figure 7.** SEM images of: (a, b) of the left-handed HNFs of (*mR,pS*)-**5** (free surface in (a) and confined to 60 nm channel AAO in (b)) and (c, d) and of the right-handed HNFs of (*mS,pR*)-**5** (free surface in (c) and confined to 60 nm channel AAO in (d)). Scale bars are 500 nm, except in the magnified section on the right, where they are 250 nm. The 3D model in each (b) and (d) shows the handedness of the confined HNFs, whose shape appears to have changed now featuring a smaller helical pitch of ~ 100 nm.

**Figure 8.** (a, b) Low-dose TEM images taken from two locations on the TEM grid of right-handed HNFs formed by (*mS,pR*)-**5** (scale bar: 200 nm).

**Figure 9.** Tapping mode AFM images of left-handed HNFs formed by ( $^mR,^pS$ )-**5** on cooling at a rate of  $5\text{ }^\circ\text{C min}^{-1}$  from the isotropic liquid phase to room temperature ( $\sim 20\text{ }^\circ\text{C}$ ): (a) 2D topographical image (scale bar: 500 nm) and (b) 3D topographic image. Although more difficult to clearly discern in comparison to the SEM images, some areas with identifiable left-handed HNFs are traced in each image by a white dashed line.

**Figure 10.** Lowest energy geometries obtained at the B3LYP/6-311(d,p) level of theory for: (a) ( $^mR,^pS$ )-**5** and (b) ( $^mS,^pR$ )-**5**.

**Figure 11.** (a) Chemical structure and definitions of dihedrals analyzed for ( $^mR,^pS$ )-**5** and ( $^mS,^pR$ )-**5**. Dihedral distribution functions for selected dihedrals for: (b) ( $^mS,^pR$ )-**5** and (c) ( $^mR,^pS$ )-**5**. (d) *para*-Side biphenyl torsion angle distributions  $\omega_1$  and  $\omega_2$  of ( $^mS,^pR$ )-**5**.

**Figure 12.** Graphical summary of the effect of number, configuration, and position of chiral center(s) in the aliphatic side chains of this-biphenyl diester BCLCs: compared are only those B4 filament morphologies with negative Gaussian curvature, the dimensions of the HLNCs are on the order of the  $\text{HNF}_{\text{mod2bS}}$ .

TOC Entry

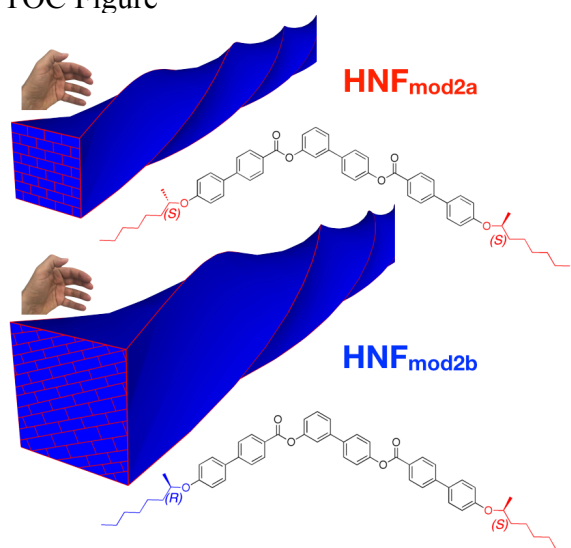
**Precisely between nano and micro.** By positioning chiral centers in the aliphatic side chains of asymmetric bent-core liquid crystals, thereby strategically introducing chiral centers, leads to yet another morphology for the B4 phase, which, with respect to width and helical pitch, occupies the place right between helical nano- and helical microfilaments. This morphology also features a new internal structure not seen before for B4 phase morphologies.

**Keyword:** hierarchical self-assembly, chirality, helical nanofilaments, bent-core liquid crystals, curvature, B4 phase.

Sasan Shadpour, Ahlam Nemati, Mirosław Salamończyk, Marianne E. Prévôt, Jiao Liu, Nicola J. Boyd, Mark R. Wilson, Chenhui Zhu, Elda Hegmann, Antal I. Jákli, Torsten Hegmann\*

### The B4 Phase of Non-Symmetrical Bent-core Liquid Crystals with Two Chiral Side Chains: Which Chiral Center Controls the Helical Nanofilament Handedness?

TOC Figure



## Supporting Information

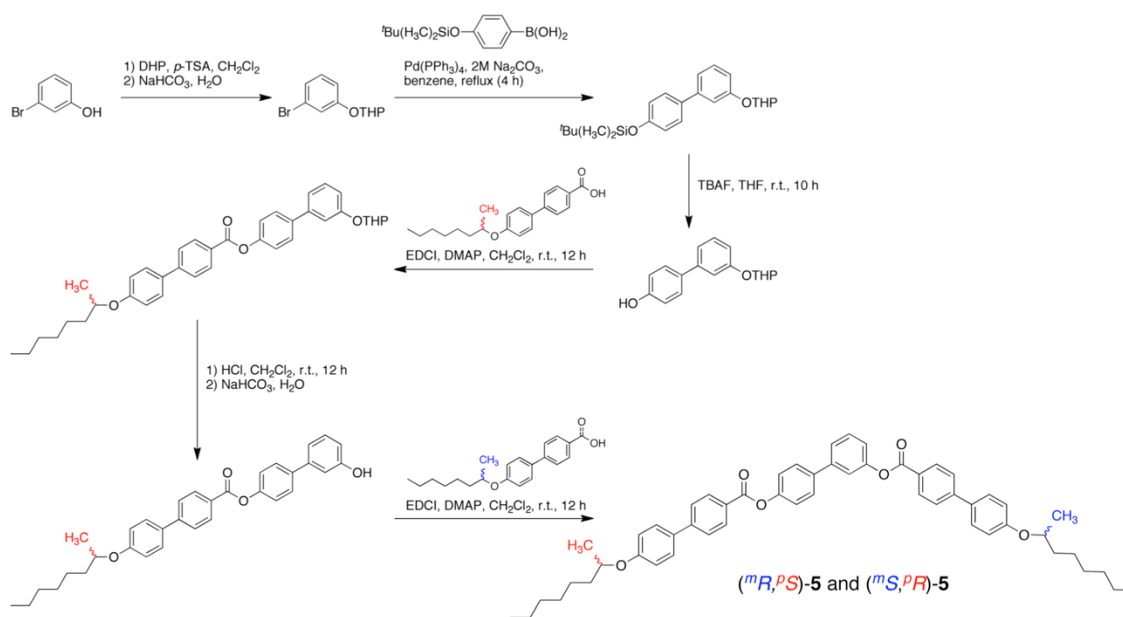
**Missing Link between Helical Nano- and Microfilaments in B4 Phase Bent-Core Liquid Crystals, and Deciphering which Chiral Center Controls the Filament Handedness**

*Sasan Shadpour<sup>a</sup>, Ahlam Nemati<sup>a</sup>, Mirosław Salamończyk<sup>b</sup>, Marianne E. Prévôt, Jiao Liu<sup>a</sup>, Nicola J. Boyd<sup>c</sup>, Mark R. Wilson<sup>c</sup>, Chenhui Zhu<sup>d</sup>, Elda Hegmann<sup>a,e,f</sup>, Antal I. Jákli<sup>a,g</sup>, Torsten Hegmann<sup>a,f,h</sup>*

*<sup>a</sup> Chemical Physics Interdisciplinary Program, Advanced Materials and Liquid Crystal Institute, Kent State University, Kent (OH) 44242-0001, USA; <sup>b</sup> Faculty of Chemistry, University of Warsaw, 02-089 Warszawa, Poland; <sup>c</sup> Department of Chemistry, Durham University, Durham, DH1 3LE, UK; <sup>d</sup> Advanced Light Source, Lawrence Berkeley National Laboratory, Berkeley, CA, 94720, USA; <sup>e</sup> Department of Biological Sciences, Kent State University, Kent (OH) 44242-0001, USA; <sup>f</sup> Brain Health Research Institute, Kent State University, Kent (OH) 44242-0001, USA; <sup>g</sup> Department of Physics and Astronomy, Kent State University, Kent (OH) 44242-0001, USA; <sup>h</sup> Department of Chemistry and Biochemistry, Kent State University, Kent (OH) 44242-0001, USA*

Contact: [thegmann@kent.edu](mailto:thegmann@kent.edu)

## SYNTHESIS



**Scheme S1.** Synthetic route pursued to obtain compounds (*<sup>m</sup>R*,*<sup>p</sup>S*)-5 and (*<sup>m</sup>S*,*<sup>p</sup>R*)-5.

**4'-[4-(2-(*R*)-heptan-2-yloxy)biphenyloxy]-3-[4-(4'-[2-(*S*)-heptan-2-yloxy)biphenyloxy]biphenyl (*<sup>m</sup>S*,*<sup>p</sup>R*)-5:**

In a N<sub>2</sub>-purged flask, 4'-[4-(2-(*R*)-heptan-2-yloxy)biphenyloxy]-3-hydroxybiphenyl (64 mg, 0.137 mmol), 4'-[2-(*S*)-heptan-2-yloxy]biphenyl-4-carboxylic acid (50.6 mg, 0.165 mmol), and DMAP (20.8 mg, 0.170 mmol) were dissolved in a mixture of dichloromethane (5 mL) and THF (5 mL) and stirred for 5 minutes. Then, EDCI (33.2 mg, 0.173 mmol) was added.

The reaction was kept under stirring at room temperature under N<sub>2</sub> for 18 hours and examined by TLC. The resulting mixture was washed with saturated NaCl solution, extracted with CHCl<sub>3</sub>, and then dried over anhydrous Na<sub>2</sub>SO<sub>4</sub>. The filtrate was collected by filtration and concentrated by rotary evaporation under reduced pressure. The residue was deposited onto silica and purified by column chromatography with CHCl<sub>3</sub> to yield a white solid (109 mg, 99%).

$^1\text{H}$  NMR (400 MHz,  $\text{CDCl}_3$ ):  $\delta$  8.30 (dd, 4H,  $J = 8.3, 4.9$  Hz, biphenyl), 7.74 (dd, 6H,  $J = 8.5, 2.1$  Hz, biphenyl), 7.64 (dd, 4H,  $J = 8.7, 3.8$  Hz, biphenyl), 7.57 – 7.50 (m, 3H, biphenyl), 7.36 (d, 2H,  $J = 8.6$  Hz, biphenyl), 7.29 (s, 1H, biphenyl), 7.04 (dd, 4H,  $J = 8.6, 5.9$  Hz, biphenyl), 4.46-4.39 (q, 1H+1H,  $J = 6.1$  Hz,  $-\text{OCHCH}_3-$ ,  $-\text{CHCH}_3$ ), 1.86 (s, 2H+1H,  $-\text{OCH}_2\text{CH}_2\text{C}_6\text{H}_{13}$ ,  $-\text{OCHCH}_3\text{CH}^a\text{CH}^b$ ), 1.62 (s, 1H,  $-\text{OCHCH}_3\text{CH}^a\text{CH}^b$ ), 1.52 (s, 3H), 1.43 – 1.30 (m, 18H), 0.94 (s, 3H+3H,  $J = 6.95$  Hz,  $-\text{CHCH}_3\text{CH}^a\text{H}^b\text{C}_4\text{H}_8\text{CH}_3$ ,  $\text{OC}_7\text{H}_{14}\text{CH}_3$ ).  $^{13}\text{C}$  NMR (100 MHz,  $\text{CDCl}_3$ ):  $\delta$  165.17, 159.61, 158.74, 151.46, 150.77, 146.05, 142.08, 137.97, 131.96, 131.81, 130.77, 129.86, 128.46, 128.32, 127.44, 126.63, 124.62, 122.14, 120.69, 120.51, 116.20, 115.01, 77.37, 77.05, 76.73, 74.05, 68.19, 36.50, 31.86, 29.40, 29.28, 26.09, 25.57, 22.70, 19.78, 14.15. Elemental analysis: Calculated for  $\text{C}_{54}\text{H}_{58}\text{O}_6$ : C, 80.77; H, 7.28. Found: C, 80.81; H, 7.67.

**4'-[4-(2-(*S*)-heptan-2-yloxy)biphenyloxy]-3-[4-(4'-[2-(*R*)-heptan-2-yloxy)biphenyloxy]biphenyl (*mR,pS*)-5:**

Compound (*mR,pS*)-**5** was synthesized following the same route as compound (*mS,pR*)-**5** above. Quantities: 4'-[4-(2-(*S*)-heptan-2-yloxy)biphenyloxy]-3-hydroxybiphenyl (64 mg, 0.137 mmol), 4'-[2-(*R*)-heptan-2-yloxy]biphenyl-4-carboxylic acid (50.6 mg, 0.165 mmol), DMAP (20.8 mg, 0.170 mmol), and EDCI (33.2 mg, 0.173 mmol). The residue was deposited onto silica and purified by column chromatography with  $\text{CHCl}_3$  to yield a white solid (90.6 mg, 84%).

**NMR SPECTRA**

Both final compounds gave exactly identical  $^1\text{H}$  and  $^{13}\text{C}$  NMR spectra.

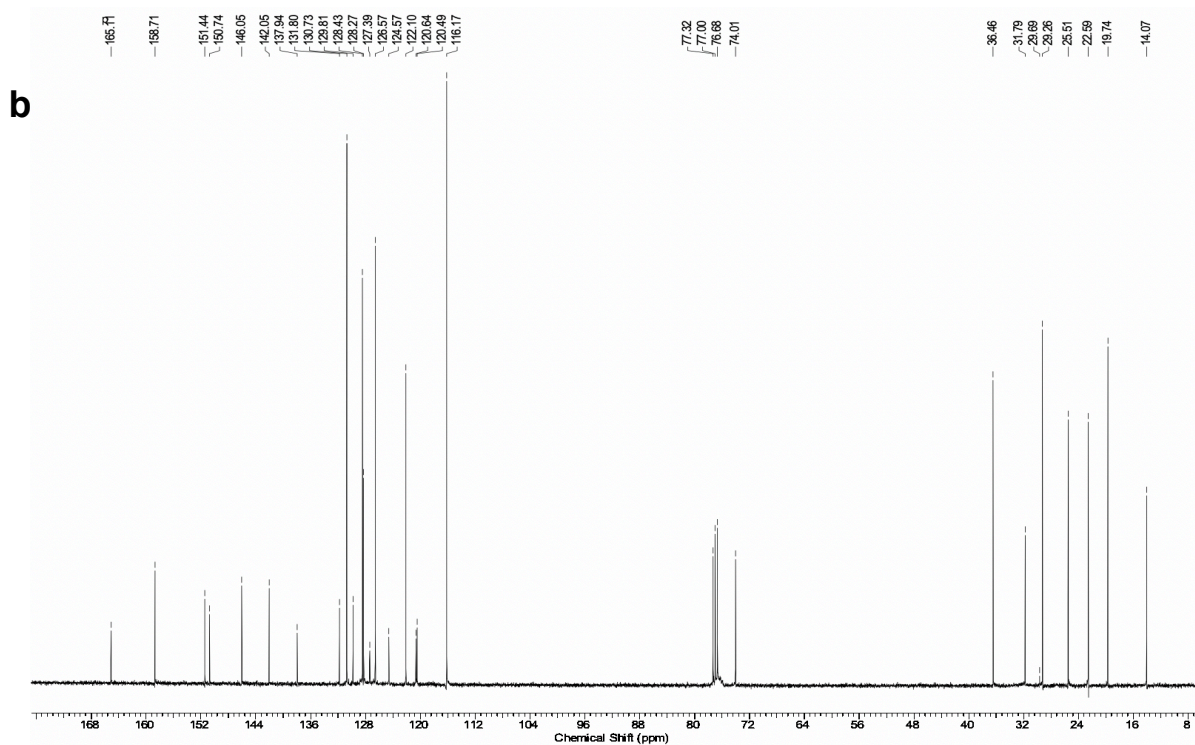
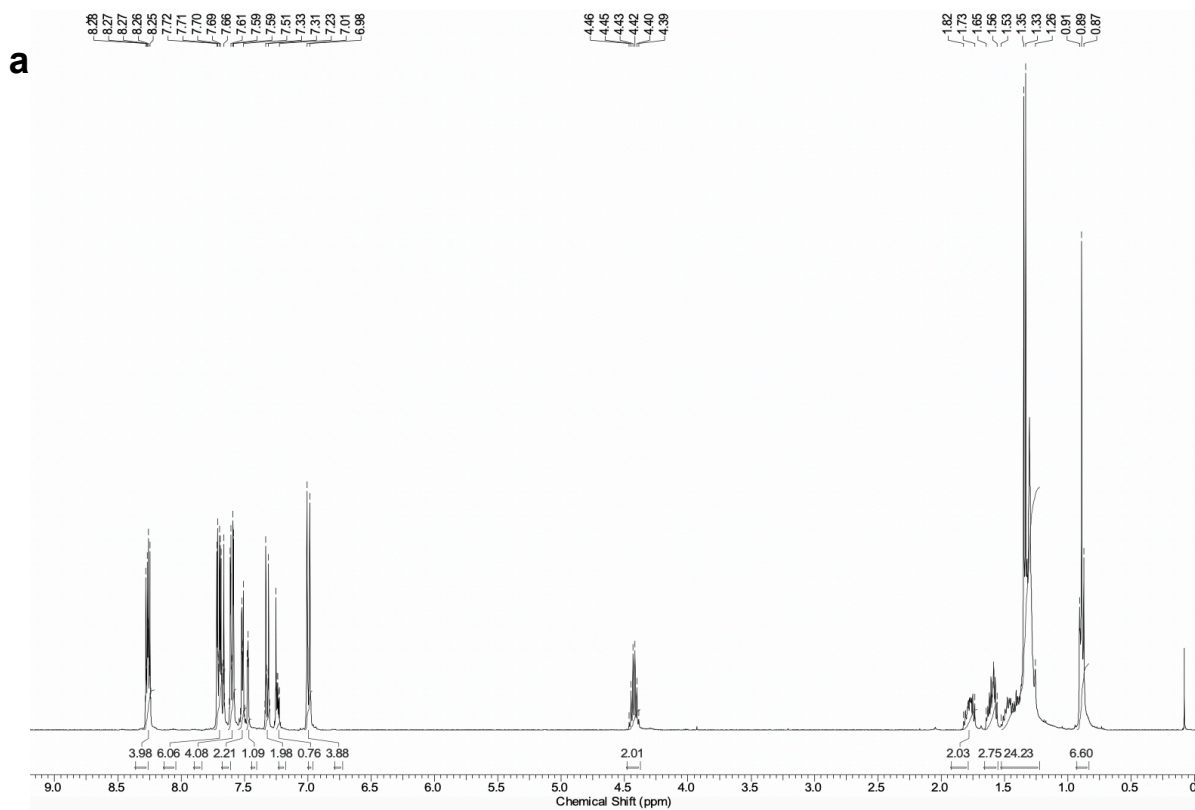


**Figure S1.** (a)  $^1\text{H}$  NMR spectrum and (b)  $^{13}\text{C}$  NMR spectrum of ( $mS,pR$ )-**5**.

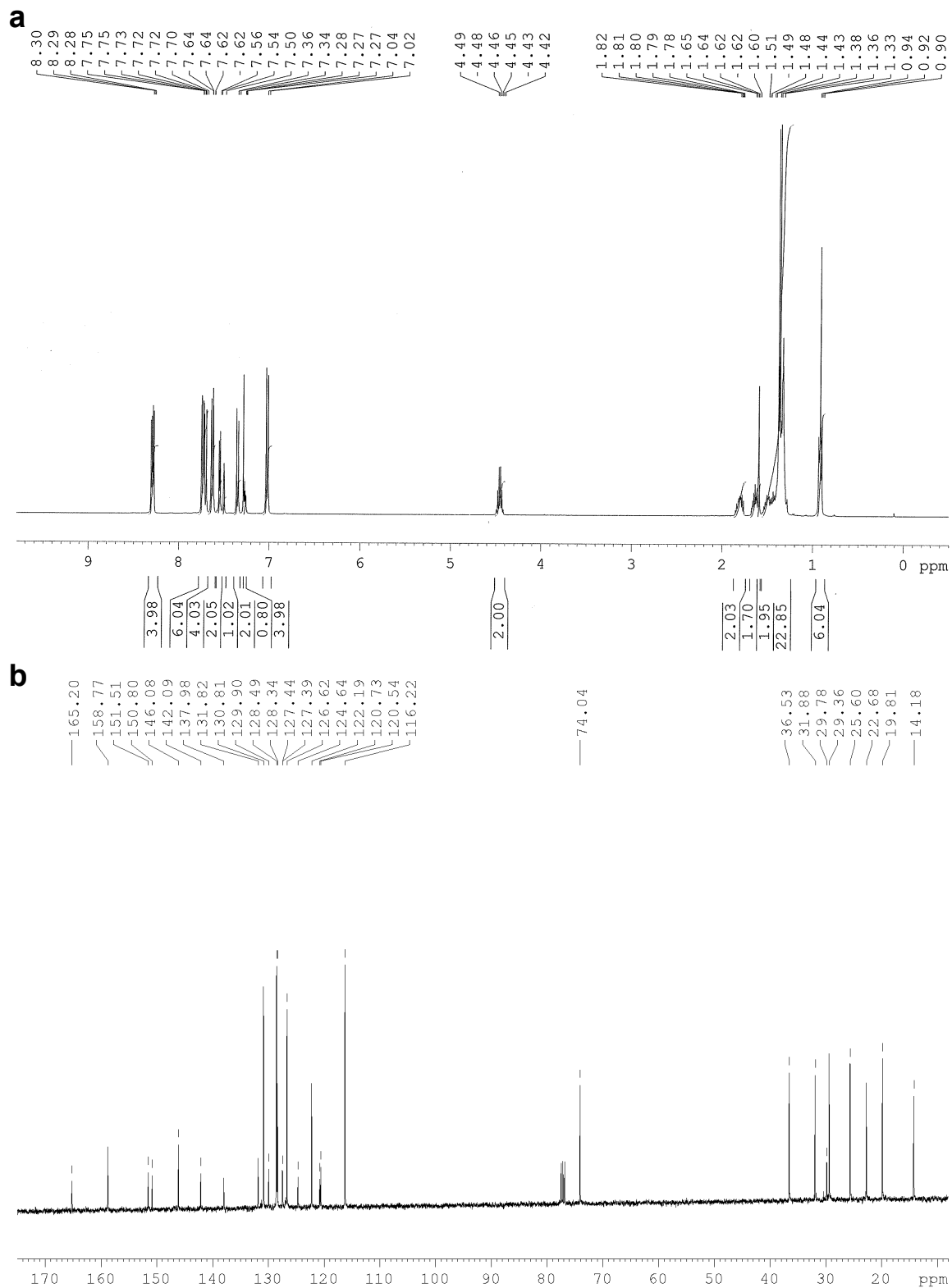


**Figure S2.** (a)  $^1\text{H}$  NMR spectrum and (b)  $^{13}\text{C}$  NMR spectrum of ( $mR,P,S$ )-5.

## ADDITIONAL POM IMAGES

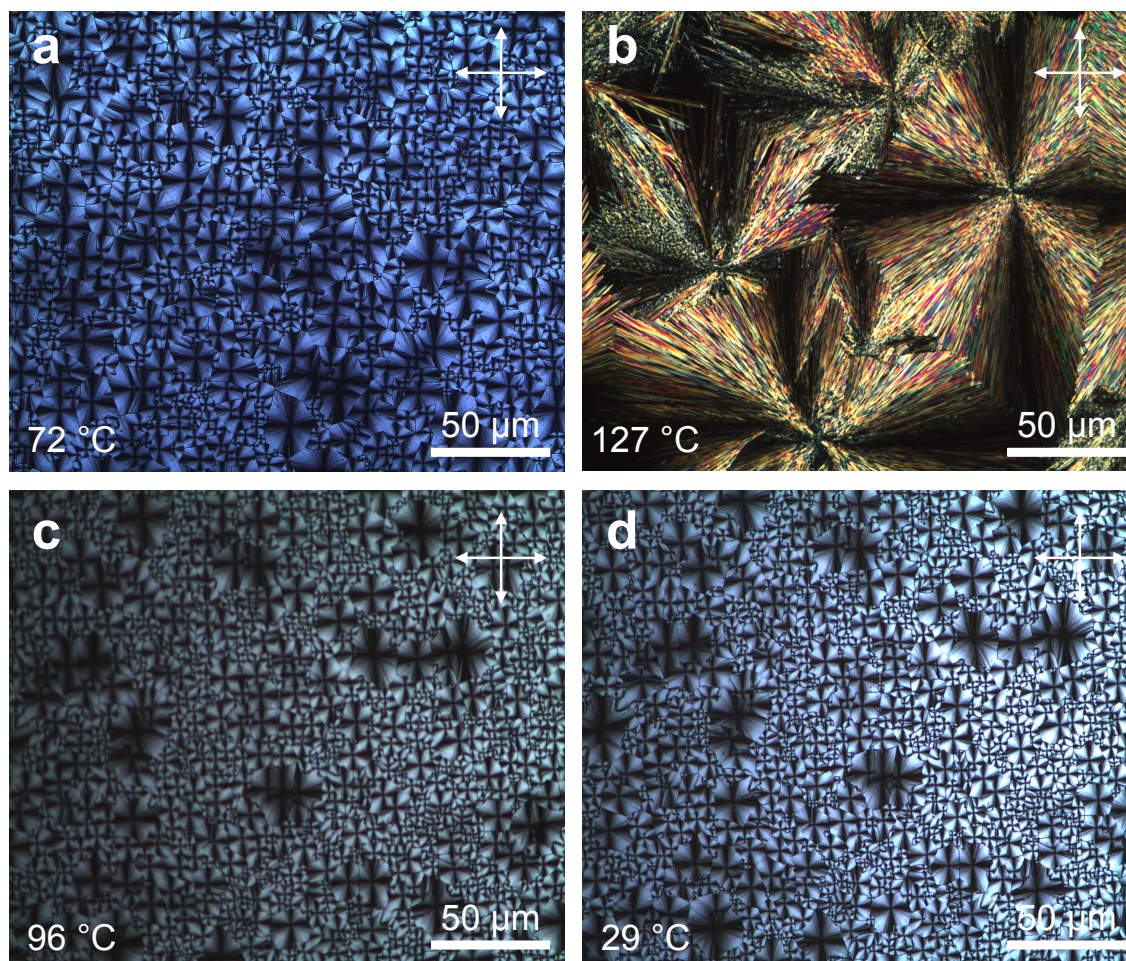


**Figure S3.** Polarized optical photomicrographs (crossed polarizers) for compound (*mS,pR*)-5 observed at heating/cooling rate of 5 °C min<sup>-1</sup>: (a, b) after first heating and cooling to room temperature the images show: (a) the HNF<sub>mod2</sub> phase and (b) the Col<sub>ob</sub> phase on second heating. On second cooling, only the HNF<sub>mod2</sub> phase was observed; see images (c) and (d). The temperatures and scale bars are indicated in each photomicrograph.

## DSC DATA

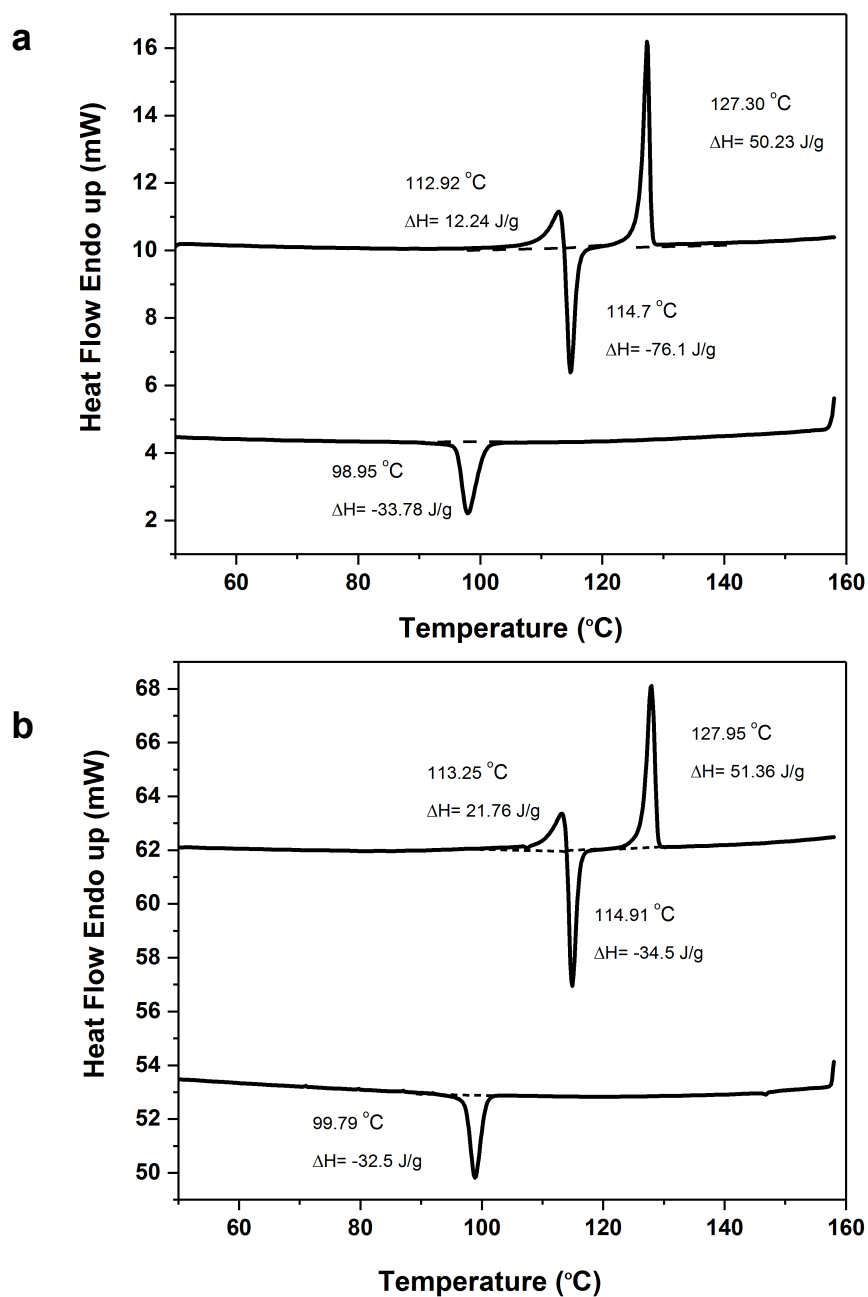


**Figure S4.** DSC plots taken directly from the Perkin Elmer Pyris 1 software interface at a rate of  $5\text{ }^{\circ}\text{C min}^{-1}$ : (a) (*mS,pR*)-**5** and (b) (*mR,pS*)-**5**. The exothermic peaks observed during the heating runs at  $\sim 114\text{ }^{\circ}\text{C}$  appear to be crystallization events at the transition from the  $\text{HNF}_{\text{mod}2}$  to the  $\text{Col}_{\text{ob}}$  phase. A similar crystallization event has been described earlier for the two derivatives with chiral centers exclusively in the *para*-side, (*pR*)-**4** and (*pS*)-**4**.<sup>[1]</sup>

## ADDITIONAL XRD DATA

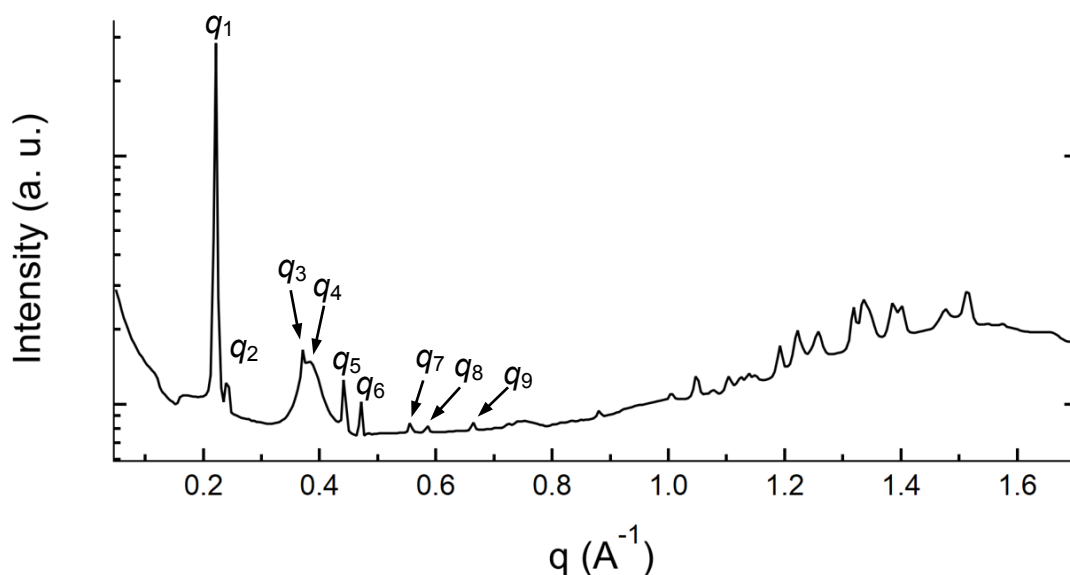


**Figure S5.** X-ray diffraction analysis of (*mS,pR*)-**5** – intensity (a.u.) vs. wave vector  $q$  ( $\text{\AA}^{-1}$ ) recorded at 120 °C (temperature range of the Col<sub>ob</sub> phase) on second heating at a rate of 5 °C min<sup>-1</sup>. The position of the peaks in the small angle region ( $q = 0.2 - 0.7 \text{ \AA}^{-1}$ ):  $q_1 = 0.22 \text{ \AA}^{-1}$ ,  $q_2 = 0.24 \text{ \AA}^{-1}$ ,  $q_3 = 0.37 \text{ \AA}^{-1}$ ,  $q_4 = 0.39 \text{ \AA}^{-1}$  (from Kapton substrates),  $q_5 = 0.44 \text{ \AA}^{-1}$ ,  $q_6 = 0.47 \text{ \AA}^{-1}$ ,  $q_7 = 0.55 \text{ \AA}^{-1}$ ,  $q_8 = 0.59 \text{ \AA}^{-1}$ , and  $q_9 = 0.66 \text{ \AA}^{-1}$ .

## ADDITIONAL GEL CD DATA

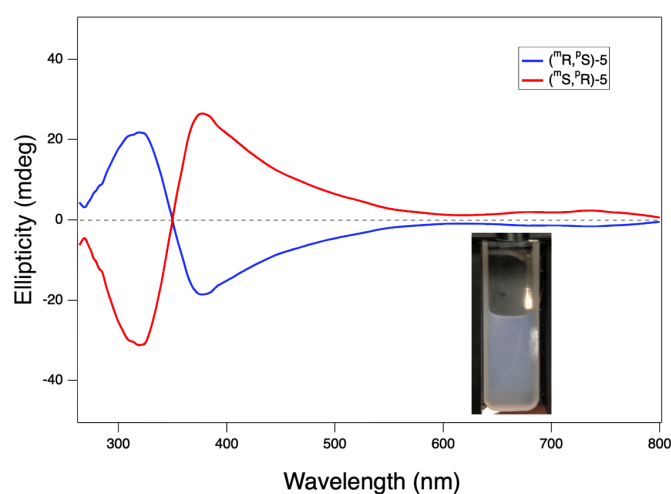


**Figure S6.** Solution (gel) CD spectra of (*mS,pR*)-**5** and (*mR,pS*)-**5** recorded in toluene at a concentration of  $\sim 4 \text{ mg mL}^{-1}$ . Inset shows the faint blue structural color indicating the formation of HNF<sub>mod2bS</sub> in toluene.

## COMPUTATIONAL METHODS

All the atomistic calculations were performed using the GROMACS 4.6.7 [2] package with a modified GAFF force field (GAFF-LCFF) developed earlier [3,4]. The energy function employed in the calculations is given by the equation:

$$\begin{aligned}
 E^{MM} = & \sum_{bonds} K_r (r - r_{eq})^2 + \sum_{angles} K_\theta (\theta - \theta_{eq})^2 + \sum_{n=0}^5 C_n (\cos(\psi))^n \\
 & + \sum_{impropers} K_d (1 + \cos(n_d \omega - \omega_d)) \\
 & + \sum_{i>j}^N \left[ 4\varepsilon_{ij} \left( \left( \frac{\sigma_{ij}}{r_{ij}} \right)^{12} - \left( \frac{\sigma_{ij}}{r_{ij}} \right)^6 \right) + \frac{1}{4\pi\varepsilon_0} \frac{q_i q_j}{r_{ij}} \right], \quad \text{Equation 1}
 \end{aligned}$$

where  $r_{eq}$ ,  $\theta_{eq}$  are structural equilibration parameters,  $K_r$ ,  $K_\theta$  and  $C_n$  are force constants,  $\varepsilon_{ij}$  and  $\sigma_{ij}$  are the usual Lennard-Jones parameters and  $q_i$  and  $q_j$  are partial electronic charges.

Changes in  $E^{MM}$  arising from deviations in improper dihedral angles,  $\omega$ , are represented by cosine functions using the force constants,  $K_d$ , the harmonic coefficients,  $n_d$ , and the phase angles,  $\omega_d$ . Throughout this work these improper dihedral angle parameters have been applied unchanged from the original GAFF force field. The standard Lorentz-Berthelot mixing rules of  $\varepsilon_{ij} = (\varepsilon_i)^{1/2}(\varepsilon_j)^{1/2}$  and  $\sigma_i = (\sigma_i + \sigma_j)/2$  have been applied for calculating the LJ parameters between different types of atoms. All molecules selected for these studies were built using the AVOGADRO 1.0.0 program. The OpenBabel code was used to extract coordinate files including the connectivity information. The Antechamber software from AmberTools 1.4 was used to generate GAFF topologies, with the point charges derived through the AMI-BCC method. The GAFF topologies and coordinate files were converted into the GROMACS format using the acpype\_py script [5]. Single molecule stochastic dynamics (SD) atomistic simulations were performed for each mesogen in the gas phase, at 300 K and for a total of 500 ns. The geometry of each mesogen was optimized in vacuum

using DFT methods and the B3LYP hybrid atfunctional, combined with the 6-311G(d,p) basis set.

### ELECTRO-OPTIC TESTS

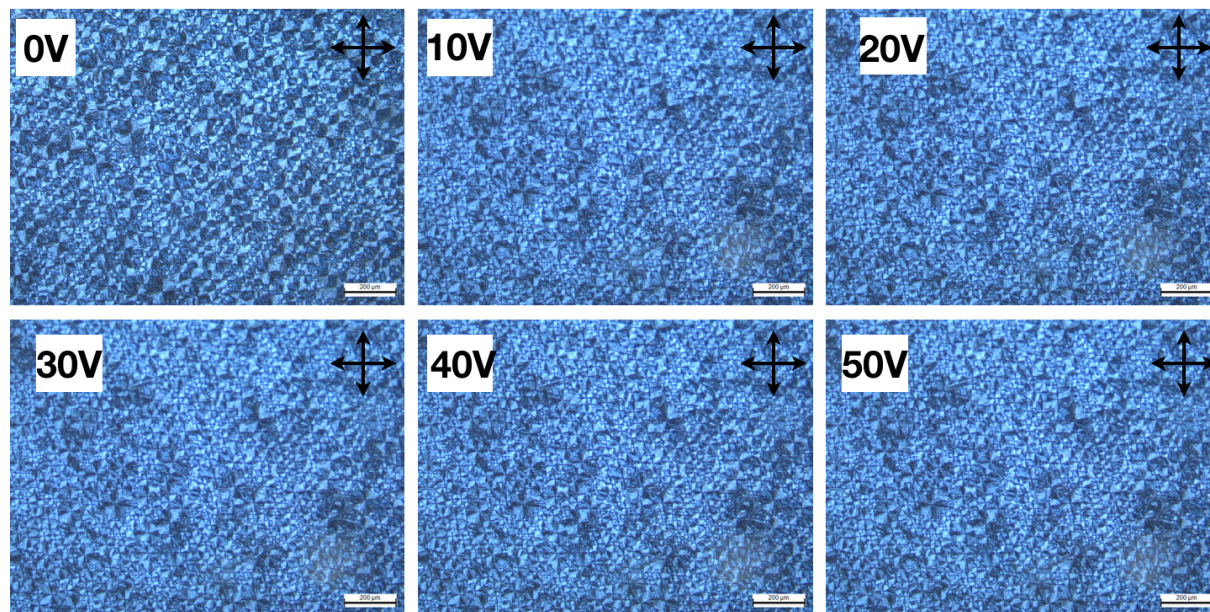


**Figure S7.** Polarized optical photomicrographs of ( $^mS,^pR$ )-5 sandwiched in ITO-coated glass cell (cell gap: 5  $\mu\text{m}$ ) with rubbed polyimide alignment layers inducing planar alignment photographed after stepwise increasing the applied electric field. The texture closely resembles the texture observed between plain glass slides, and only a minor change in the birefringence is observed upon applying any electric field. Scale bars: 200  $\mu\text{m}$ ; crossed polarizers.

### REFERENCES

- [1] S. Shadpour, A. Nemati, N. J. Boyd, L. Li, M. E. Prévôt, S. L. Wakerlin, J. P. Vanegas, M. Salamończyk, E. Hegmann, C. Zhu, M. R. Wilson, A. I. Jákli, T. Hegmann, *Mater. Horiz.* **2019**, *6*, 959-968.
- [2] S. Pronk, S. Pall, R. Schulz, P. Larsson, P. Bjelkmar, R. Apostolov, M. R. Shirts, J. C. Smith, P. M. Kasson, D. van der Spoel, B. Hess, E. Lindahl, *Bioinformatics*, **2013**, *29*, 845-854.
- [3] N. J. Boyd, M. R. Wilson, *Phys. Chem. Chem. Phys.*, **2015**, *17*, 24851-24865.
- [4] N. J. Boyd, M. R. Wilson, *Phys. Chem. Chem. Phys.*, **2018**, *20*, 1485-1496.
- [5] A. W. Sousa da Silva, W. F. Vranken, *BMC Research Notes*, **2012**, *5*, 367.